RSC Advances

PAPER

View Article Online
View Journal | View Issue

Cite this: *RSC Adv.*, 2025, **15**, 28703

Al and Ti-doped black phosphorus as sensitive materials for adsorption of HF and H_2S toxic gases: an *ab initio* study

Rashek Dewan Daymond, Fatin Hasnat Shihab, Nihal Siddique, Mohammad Tanvir Ahmed, Abdullah Al Roman and Debashis Roy *

This study explores the potential of aluminum (Al) and titanium (Ti)-doped black phosphorus (BP) as sensitive materials for detecting and adsorbing toxic gases, hydrogen fluoride (HF) and hydrogen sulfide (H_2S), using Density Functional Theory (DFT) calculations. The structural, electronic, and optical properties of pristine BP, Al and Ti-doped BP before and after gas adsorption were investigated. Molecular dynamics revealed the thermodynamic stability of all the substrates at room temperature. Al and Ti-doping enhanced the adsorption behavior of BP significantly. The studied adsorbents revealed both physisorption and chemisorption of the selected gases, with maximum adsorption energy of −1.651 eV for HF gas. Electronic analyses show that Ti-doping transforms BP into a metal, while Al-doping modulates the band gap, improving sensitivity. Charge distribution indicates significant electron redistribution in doped systems upon gas adsorption. Additionally, optical spectra show slight red shifts due to gas adsorption. RGD analysis revealed the presence of weak van der Waals and strong attractive interactions between adsorbents and the gas molecules. The findings indicate that Al and Ti-doped BP are promising materials for the development of highly sensitive and selective gas sensors targeting HF and H_2S molecules.

Received 7th July 2025
Accepted 5th August 2025

DOI: 10.1039/d5ra04844c

rsc.li/rsc-advances

1. Introduction

A balanced composition of gases in Earth's atmosphere is crucial for sustaining all life. But this balance is increasingly disrupted by population growth, industrialization, transportation, and other anthropogenic activities.[1] The environment is contaminated by a variety of toxic gases, such as hydrogen sulfide (H_2S), hydrogen fluoride (HF), hydrogen cyanide (HCN), ozone (O_3), carbon monoxide (CO), nitrogen dioxide (NO_2), sulfur dioxide (SO_2) and so on, harming the ecosystem and affecting human health.[2,3] Here, HF and H_2S are poisonous, colorless gases commonly found in industrial and environmental contaminants.[4] Furthermore, H_2S is a flammable, toxic gas that smells like rotten eggs and is extremely corrosive under ambient conditions, which can easily damage the human nervous system.[5,6] To ensure safety for health, a person's exposures to H_2S gas should not exceed 15 ppm for 10 minutes or 10 ppm for 8 hours duration.[7] Conversely, HF is a toxic, corrosive, and odorous gas that boils near room temperature, and its aqueous form, hydrofluoric acid, is a key source of fluorine.[8] According to the toxicity of HF gas, it irritates the respiratory tract at low concentrations, and when inhaled, it can spread throughout the tissues and bones, leading to skeletal fluorosis and even potentially death.[9] Therefore, to ensure the safety of human life and the environment, the development of reliable, efficient, and cost-effective gas sensors is required for the detection and adsorption of hazardous gas molecules.[10]

Two-dimensional (2D) materials are extensively researched for numerous applications, especially gas sensors, energy storage, electronic devices, biomedical sector, and so on.[11,12] Their exceptional properties, such as nanoscale thickness, high surface area to volume ratio, unique electronic properties, and excellent optical properties, significantly enhance their sensitivity and response times.[13,14] Nowadays, 2D nanomaterials with layered structures, including graphene, transition-metal dichalcogenides (TMDCs), black phosphorus, hexagonal boron nitride (h-BN), and MXenes, have been identified as effective gas sensors, capable of operating efficiently at low or ambient temperatures.[15] Graphene was first isolated by Geim and Novoselov from Manchester University in 2004 through mechanical exfoliation.[16] In prior research, the sensing capabilities of graphene for chemicals like CO_2, CO, NO_2, NH_3, and H_2O have been reported.[17,18] Despite the numerous benefits of graphene, it also exhibits inherent defects, including a chemically inert surface and zero band gap, as well as poor sensitivity.[19,20]

Condensed Matter Physics Lab (CMP Lab), Department of Physics, Jashore University of Science and Technology, Jashore-7408, Bangladesh. E-mail: debashisroy41ju@gmail.com

BP demonstrates superior efficiency in gas sensing compared to other 2D materials due to its exceptional properties, including puckered hexagonal structure, high surface-to-volume ratio, high adsorption energy, direct bandgap, high carrier mobility (~1000 $cm^2 V^{-1} s^{-1}$) at room temperature, an excellent on/off current ratio, and so on.[21–23] BP is intrinsically a p-type semiconducting material. It is the most thermodynamically stable allotrope of phosphorus, surpassing red, white, and violet varieties.[24] Additionally, BP is synthesized from both white and red allotropes of phosphorus, and Bridgman achieved the first successful synthesis of BP in 1914 by transforming white phosphorus at 1.2 GPa pressure and 200 °C temperature.[25] The weak van der Waals forces in the stacked interlayer structure of BP enable the production of ultrathin nanosheets through mechanical or liquid exfoliation from bulk BP crystals.[26] Recently, BP is increasingly being used in various sectors, including gas sensors, optoelectronics, energy storage, batteries, transistors, solar cells, supercapacitors, photodetectors, and so on.[27] Few studies have been conducted on BP and modified BP regarding the adsorption of gas molecules.[28] For instance, Lalitha *et al.* theoretically investigated the adsorption of NH_3, H_2, CO_2, and CH_4 gases on pristine, Ca-doped, and Ca-functionalized BP.[29] Another investigation into the adsorption of CO, CO_2, NH_3, and NO_2 on graphene, MoS_2, and BP demonstrated that BP had the strongest affinity for these gases.[30] According to Kou *et al.*, the adsorption energy and current–voltage behavior of BP were calculated upon exposure to several gases, as well as Cho *et al.* highlighted BP's unique sensing ability over MoS_2 and graphene.[31,32] Additionally, a study explored the H_2 gas sensing capabilities of BP doped with Ni, Pd, and Pt, focusing on its adsorption behavior.[33] The adsorption energies for NH_3, CH_4, and H_2O are notably enhanced on In-doped BP compared to pure BP.[34] As a result, Li-doped BP exhibits the most optimal adsorption energy for a range of gases (CO, CO_2, NO_2, and SO_2), surpassing the adsorption performance of Na, K, Rb, and Cs.[35] Previous studies have demonstrated that point defects in BP enhance adsorption energies and selectivity for toxic gases like NO_2 and SO_2, while showing low sensitivity to less reactive gases such as CO, CO_2, and NH_3.[36] According to Chen *et al.*, Li-decorated N-doped BP exhibits an adsorption strength sequence of $H_2S < SO_2 < NO_2$, with NO_2 showing the strongest chemisorption due to significant orbital hybridization.[37] Yang *et al.*, also reported that pristine and Au-doped α-phase black arsenic phosphorus monolayers are stable and exhibit strong adsorption toward CO, NO_2, and NO gases.[38] In addition, Fe-decorated blue phosphorene exhibits strong CH_4 adsorption and high sensitivity due to its modified electronic and magnetic properties.[39] Recent advances have demonstrated that Pt-decorated BP–WS_2 heterostructure sensors overcome the typical limitations of TMD devices, providing enhanced NO_2 sensitivity and improved recovery at low temperatures.[40] Balaji *et al.* reported that the α-AsP monolayer adsorbs acetaldehyde more strongly than formaldehyde, with adsorption energies between −0.28 and −0.50 eV, suggesting its suitability for detecting volatile organic compounds.[41]

In this study, BP nanostructures were designed and doped with Al and Ti atoms. Their geometrical, optical, and electronic properties were investigated using first-principles calculations to analyze and compare their sensing potential for HF and H_2S gas molecules. To enhance the understanding of adsorption behavior, we have analyzed the molecular dynamics (MD), adsorption energies (E_{ads}), electron density difference (EDD), band structure, density of states (DOS), partial density of states (PDOS), and recovery time of the studied structures. We further conducted reduced density gradient (RDG) analysis to gain insight into the nature of the interactions between the adsorbents and the adsorbates. To the best of our knowledge, the adsorption behavior of Al and Ti-doped BP for the selected gases has not been reported yet.

2. Computational details

This study used the density functional theory (DFT) method utilizing the Cambridge Serial Total Energy Package (CASTEP).[42] This algorithm explores the geometric, electronic, and optical properties of pristine BP, Al-doped BP (Al-BP), and Ti-doped BP (Ti-BP), focusing on their interactions with HF and H_2S gas molecules. In this study, a $3 \times 3 \times 1$ supercell of BP nanosheet was modeled with the electronic configuration $[Ne]3s^2 3p^3$. All the computational calculations were carried out using a 500 eV cutoff energy and $3 \times 3 \times 1$ uniform *k*-mesh, while the exchange–correlation potential was addressed *via* Perdew–Burke–Ernzerhof (PBE) functional within the Generalized Gradient Approximation (GGA).[43] To eliminate interlayer interactions, a vacuum spacing of 20 Å was introduced along the *z*-axis. For the entire simulation, ultrasoft pseudo-potentials were employed, and Grimme's dispersion correction (DFT-D2) scheme was included to address long-range van der Waals interactions.[44] For the self-consistent estimation, the total energy must converge to (1×10^{-5}) eV per atom, with maximum forces of 0.03 eV $Å^{-1}$, maximum displacements of 0.001 Å, and stress not exceeding 0.05 GPa. Molecular dynamics simulations were conducted in the microcanonical (*NVE*) ensemble at 298 K for 10 picoseconds using the Forcite module to assess the dynamic stability of the studied nanosheets.[45] Additionally, the nature of the interaction between the adsorbents and adsorbates was investigated through reduced density gradient (RDG) analysis performed with VMD and Multiwfn software.[46,47]

3. Results and discussion

3.1 Geometry analysis

Structural stability is a fundamental property that governs the practical applicability of materials.[48] In this study, we designed a BP nanosheet model consisting of 42 atoms and investigated its interactions with HF and H_2S gas molecules. A single phosphorus atom was substituted by either Al or Ti, corresponding to a dopant concentration of approximately 2.38%. Additionally, the stability and structural integrity of the systems were analyzed using molecular dynamics simulations. Fig. 1 illustrates the side and top views of the optimized structures of pristine BP, metal-doped BP (Al, Ti), and their corresponding

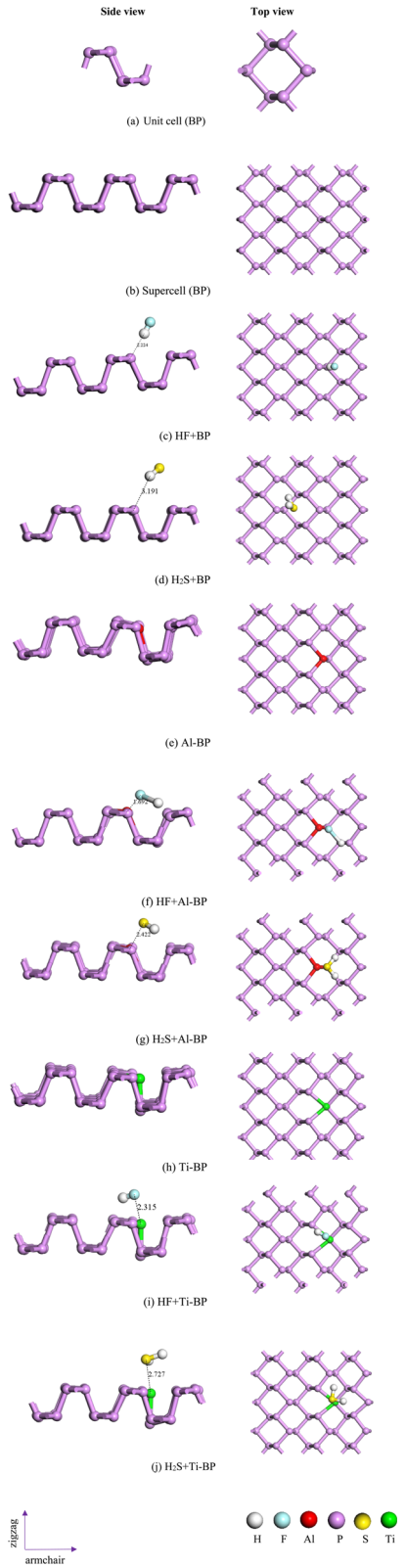

Fig. 1 Optimized side and top views of (a) unit cell (BP), (b) supercell (BP), (c) HF + BP, (d) H_2S + BP, (e) Al-BP, (f) HF + Al-BP, (g) H_2S + Al-BP, (h) Ti-BP, (i) HF + Ti-BP, and (j) H_2S + Ti-BP.

Table 1 Average bond distances for pristine and gas–adsorbed configurations

	Bond type				
Structure	P–P (Å)	Ti–P (Å)	Al–P (Å)	H–F (Å)	H–S (Å)
BP	2.219	—	—	—	—
HF + BP	2.215	—	—	0.969 (0.949)	—
H_2S + BP	2.214	—	—	—	1.350 (1.351)
Al-BP	2.215	—	2.363	—	—
HF + Al-BP	2.212	—	2.351	2.126	—
H_2S + Al-BP	2.212	—	2.325	—	1.393
Ti-BP	2.204	2.435	—	—	—
HF + Ti-BP	2.202	2.473	—	0.997	—
H_2S + Ti-BP	2.201	2.473	—	—	1.357

gas–adsorbed configurations. The average bond lengths of pristine BP, modified BP, and their gas–adsorbed complexes are summarized in Table 1. For pristine BP, the average P–P bond length was calculated to be 2.219 Å, corresponding closely to the literature value of 2.22 Å.[49,50] The calculated bond lengths for the optimized gas molecules HF and H_2S are 0.949 Å for the H–F bond and 1.351 Å for the H–S bond, respectively. These results are in agreement with previous studies.[51,52] We observed slight variations in the P–P bond lengths upon adsorption of HF and H_2S gas molecules. Specifically, the P–P bond length decreased by approximately 0.18% for HF + BP and by 0.23% for H_2S + BP, indicating minimal structural distortion due to gas adsorption. The presence of dopants such as Al and Ti further altered the bond lengths. The Al–P bond length was measured to be 2.363 Å, whereas the Ti–P bond length was recorded as 2.435 Å. Compared to pristine BP, the P–P bond length decreased by approximately 0.18% and 0.68% in the Al-BP and Ti-BP complexes, respectively. Due to gas adsorption, the Al–P bond length decreased slightly by approximately 0.51% in the HF + Al-BP complex and 1.61% in the H_2S + Al-BP complex, compared to the Al–P bond length of 2.363 Å in pristine Al-BP. In both cases, the P–P bond length remained unchanged at 2.212 Å. Similarly, a modest decrease in the P–P bond length was observed, by approximately 0.09% in HF + Ti-BP and 0.14% in H_2S + Ti-BP, relative to the P–P bond length in pristine Ti-BP. The Ti–P bond length remained constant at 2.473 Å in both systems. Furthermore, we observed that the H–F bond lengths increased across all gas–adsorbed complexes, while the H–S bond lengths increased in all cases except the H_2S + BP complex. These findings provide valuable insights into the interaction mechanisms between the adsorbents and the adsorbates.

3.2 Molecular dynamics

Molecular dynamics (MD) is a widely used computational technique for simulating and analyzing the time-dependent motions and interactions of atoms and molecules at the atomic scale.[53] This technique facilitates the understanding of how slight modifications in molecular arrangement or temperature conditions influence material properties, including sensitivity and overall stability. In this study, MD simulations were performed under the microcanonical (*NVE*) ensemble at room temperature

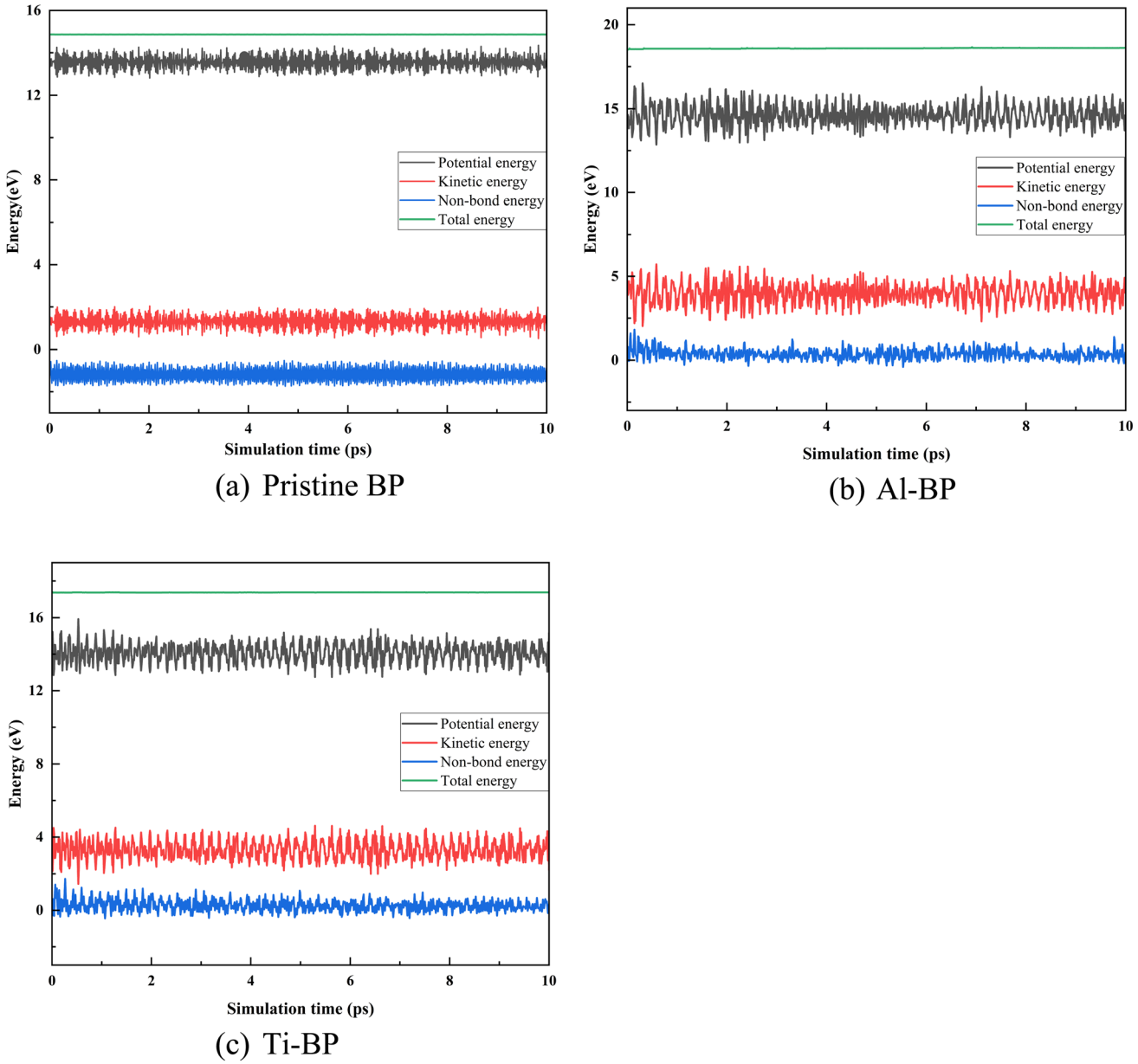

Fig. 2 Schematic representation of molecular dynamics simulations for (a) pristine BP, (b) Al-doped BP, and (c) Ti-doped BP.

(298 K) for duration of 10 picoseconds (ps) to evaluate the dynamic stability of pristine BP, as well as Al and Ti-doped BP. Fig. 2 shows the corresponding changes in potential, kinetic, non-bonded, and total energies as a function of simulation time. The fluctuations in total energy, expressed in eV, provide insights into the systems' stability and response to thermal perturbations. In Fig. 2, the MD profile of pristine BP shows a relatively stable total energy trend, with only minor fluctuations (approximately 0.05%) observed throughout the simulation period. The minimal energy fluctuations indicate strong structural integrity and effective resistance to thermal perturbations. In the case of Al-doped BP, the total energy fluctuates by about 0.61%, suggesting that the simulation model effectively captures the system's dynamic behavior. As shown in Fig. 2, the Ti-doped BP system reveals stable energy fluctuations without noticeable drift or discontinuity. The fluctuation range (approximately 0.03%) indicates that the system has attained energy equilibrium. The energy curves of the investigated systems showed fluctuations below 5%, demonstrating that all three configurations—pristine BP, Al-doped BP, and Ti-doped BP—exhibit thermal stability at 298 K.[54,55]

3.3 Adsorption energy

The adsorption energy (E_{ads}) characterizes the interaction strength between gas molecules and the substrate surface.[56] In this study, adsorption energies (E_{ads}), adsorption distances (AD), and recovery times for HF and H_2S gas molecules on pristine and metal (Al, Ti) doped BP structures were calculated, as summarized in Table 2.

Table 2 Calculated adsorption energy (E_{ads}), adsorption distance (AD), and recovery times for gas–adsorbent systems

Structure	E_{ads} (eV)	AD (Å) (before)	AD (Å) (after)	Recovery times (s)
HF + BP	−0.276	2.924	2.224	5.7×10^{-11}
H_2S + BP	−0.133	3.273	3.191	2.3×10^{-13}
HF + Al-BP	−1.651	3.433	1.692	6.7×10^{12}
H_2S + Al-BP	−0.828	3.467	2.422	1.1×10^{-1}
HF + Ti-BP	−0.502	2.415	2.315	3.5×10^{-7}
H_2S + Ti-BP	−0.584	2.896	2.727	8.5×10^{-6}

The adsorption energy was calculated using the following equation:[57]

$$E_{ads} = E_{nanosheet+gas} - E_{nanosheet} - E_{gas} \quad (1)$$

where $E_{nanosheet+gas}$ is the total energy of the nanosheets with the adsorbed gas molecule, $E_{nanosheet}$ is the energy of the pristine nanosheets, and E_{gas} is the energy of the isolated gas molecule. All systems exhibit negative adsorption energies, indicating effective molecular interaction with the material surface. We observed that the adsorption of HF on pristine BP shows higher stability relative to H_2S. Specifically, HF molecules demonstrated the strongest binding on Al-doped BP, with adsorption energy of −1.6506 eV, indicative of chemisorption. Conversely, H_2S molecules exhibited moderate physisorption interactions on the Al-doped surfaces. In contrast, pristine BP also shows relatively weaker physisorption interactions. Moreover, we observed that the adsorption energy of HF on Ti-doped BP increased by approximately 82% compared to that on pristine BP. Similarly, the adsorption energy of H_2S on Ti-doped BP was found to be −0.584 eV, indicating stronger binding than on pristine BP and highlighting the influence of Ti doping. Adsorption distances decrease with increasing adsorption energies, confirming stronger binding. For instance, HF on Al-doped BP exhibits a shorter adsorption distance (1.692 Å) compared to HF on pristine BP (2.224 Å). The highest adsorption distance was observed for H_2S on pristine BP, measuring 3.191 Å, which corresponds to its relatively lower adsorption energy. The recovery time (τ) was calculated using the expression:[57]

$$\tau = \frac{1}{f}\exp\left(\frac{-E_{ads}}{k_B T}\right) \quad (2)$$

where k_B denotes Boltzmann's constant (8.617×10^{-5} eV K^{-1}) and T is the absolute temperature. Given that sensor recovery generally occurs under UV irradiation, we considered a frequency range of (10^{12} to 3×10^{14}) Hz for the desorption process. For consistency and practical relevance, all recovery time estimations in this study were performed at a temperature of 298 K. Notably, HF adsorption on Al-doped BP results in a longer recovery time (6.74×10^{12} s) compared to other nanosheets, which remains acceptable for sensing applications.[58] In this context, regeneration of the adsorbent can be achieved through chemical treatment. The use of dilute acidic solutions, such as hydrochloric acid (HCl) or nitric acid (HNO_3), effectively facilitates the desorption process.[59] By contrast, HF and H_2S adsorption on pristine BP resulted in much faster recovery times. However, the adsorption of HF and H_2S on Ti-doped BP demonstrated reasonable recovery times, emphasizing their suitability for rapid cycling applications. These results demonstrate that doping BP sheets significantly modifies their adsorption behavior, enhancing binding strength.

3.4 Mulliken charges analysis

Mulliken charge analysis offers critical insights into the charge distribution across different atoms within a structure.[60] This

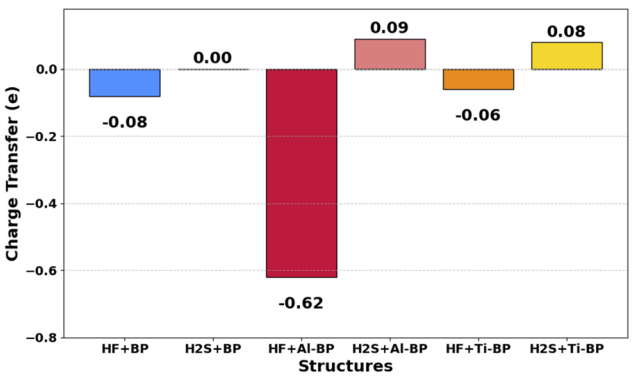

Fig. 3 Charge transfer mechanism between the adsorbent materials and the interacting gas molecules.

Table 3 Calculated average Mulliken charges of the electrons of the structures in (*e*) units

	Element					
Structure	H	F	Al	P	S	Ti
BP	—	—	—	—	—	—
HF + BP	0.550 (0.640)	−0.630 (−0.640)	—	0.002	—	—
H_2S + BP	0.195 (0.200)	—	—	−0.001	−0.390 (−0.400)	—
Al-BP	—	—	0.660	−0.018	—	—
HF + Al-BP	0.110	−0.730	1.220	−0.016	—	—
H_2S + Al-BP	0.145	—	0.780	−0.024	−0.200	—
Ti-BP	—	—	—	−0.019	—	0.690
HF + Ti-BP	0.470	−0.530	—	−0.022	—	0.800
H_2S + Ti-BP	0.155	—	—	−0.023	−0.230	0.700

helps to understand better the nature of bonding, whether ionic or covalent. In this study, we explored the Mulliken charge variations for pristine and metal-doped BP nanosheets through adsorption of HF and H_2S gas molecules, as presented in Table 3. The pristine BP structure exhibits negligible charge transfer among its constituent atoms, indicating a relatively uniform charge distribution. When HF and H_2S molecules adsorb on the BP surface, the Mulliken charges of H, F, P, and S atoms change noticeably. This shows that there is a significant transfer of charge between the gas molecules and the BP surface. Specifically, after HF adsorption, the H atom carries a positive charge of 0.55 *e* (0.64 *e* before adsorption), while the F atom attains a negative charge of −0.63 *e* (−0.64 *e* before adsorption). Similarly, H_2S adsorption results in a positive charge on H (0.195 *e*) and a negative charge on S (−0.390 *e*), respectively. In the case of Al-modified BP, the Al atom initially exhibits a charge of 0.66 *e*, which increases after HF adsorption, demonstrating significant charge redistribution. For the Ti-BP complex, Ti acquires a positive charge of 0.69 *e*, which rises by approximately 15.9% following HF adsorption and 1.5% after H_2S adsorption, suggesting enhanced interaction. Therefore, these findings confirm that electron transfer occurs between the adsorbents and the adsorbates.

The net charge transfer further confirms the interaction between the gas molecules and the nanosheets, as illustrated in Fig. 3. A positive value indicates that electrons are transferred from the gas molecule to the nanosheets, while a negative value signifies the opposite.[61]

3.5 Hirshfeld charges analysis

The Hirshfeld population analysis (HPA) technique evaluates atomic charges by distributing the deformation density among the constituent atoms in a molecular system.[62] The Hirshfeld charge analysis in Table 4 reveals that, upon adsorption of HF and H_2S gas molecules, the Al, P, and Ti atoms carry positive charges, indicating electron depletion. Conversely, the F and S atoms exhibit negative charge states, suggesting electron accumulation on the pristine and doped BP surfaces. The differences between the Hirshfeld and Mulliken analyses arise from their distinct computational approaches. However, both methods consistently reveal similar patterns of charge transfer. In Table 4, the values within parentheses represent the Hirshfeld charges before gas adsorption, while the values outside the parentheses indicate the charges after adsorption. The adsorption of HF and H_2S molecules on both pristine and metal-doped (Al, Ti) BP structures induces significant charge redistribution. This is evidenced by notable variations in Hirshfeld charge values, particularly for the H, F, and S atoms. The significant shifts in charges emphasize the strong interaction between adsorbates and BP-based substrates.

3.6 Electron density difference analysis

To visualize and better understand the charge transfer mechanisms, we analyzed the electron density difference (EDD) for both pristine and metal-doped BP upon interaction with toxic gases, as illustrated in Fig. 4. The orange regions correspond to areas of electron accumulation, whereas the blue regions indicate zones of electron deficiency. Mulliken charge analysis reveals that the EDD map illustrates the redistribution of partial atomic charges resulting from differences in electronegativity among constituent atoms within the molecule.[63,64] In pristine BP nanosheets, the electron affinity remains nearly uniform across the phosphorus lattice due to its homogeneous atomic composition, which results in minimal polarization upon gas adsorption. For HF, the minimal electron accumulation around the F atom and slight depletion near the interacting P atoms are consistent with partial charge transfer, indicating weak physisorption. Similarly, the interaction of H_2S with BP exhibits minor charge accumulation on the S atom and faint depletion at the interface, indicating a weak van der Waals interaction. With Al doping, the interaction dynamics change notably. Mulliken charge analysis shows that electrons migrate toward the more electronegative phosphorus atoms, causing charge depletion at the Al site and accumulation near neighboring P atoms. Upon HF adsorption, the highly electronegative fluorine atom strongly pulls electrons from both the H atom and the Al-doped BP surface, establishing a clear donor–acceptor interaction pathway. This indicates that HF acts as an electron acceptor while Al-doped BP donates electron density, leading to stronger chemisorption. For H_2S adsorption, sulfur exhibits moderate interaction, accompanied by electron accumulation near S and neighboring P atoms, and depletion at the Al site. This interaction indicates moderate binding; exceeding that of pristine BP. Ti-doped BP shows significant electron density changes

Table 4 Calculated average Hirshfeld charges of the electrons of the structures in (*e*) units

	Element					
Structure	H	F	Al	P	S	Ti
BP	—	—	—	—	—	—
HF + BP	0.090 (0.210)	−0.230 (−0.210)	—	0.003	—	—
H_2S + BP	0.040 (0.050)	—	—	—	−0.090 (−0.100)	—
Al-BP	—	—	0.160	−0.005	—	—
HF + Al-BP	0.020	−0.260	0.200	0.001	—	—
H_2S + Al-BP	0.030	—	0.140	−0.008	0.070	—
Ti-BP	—	—	—	−0.004	—	0.100
HF + Ti-BP	0.130	−0.110	—	−0.003	—	0.090
H_2S + Ti-BP	0.065	—	—	−0.008	0.070	0.050

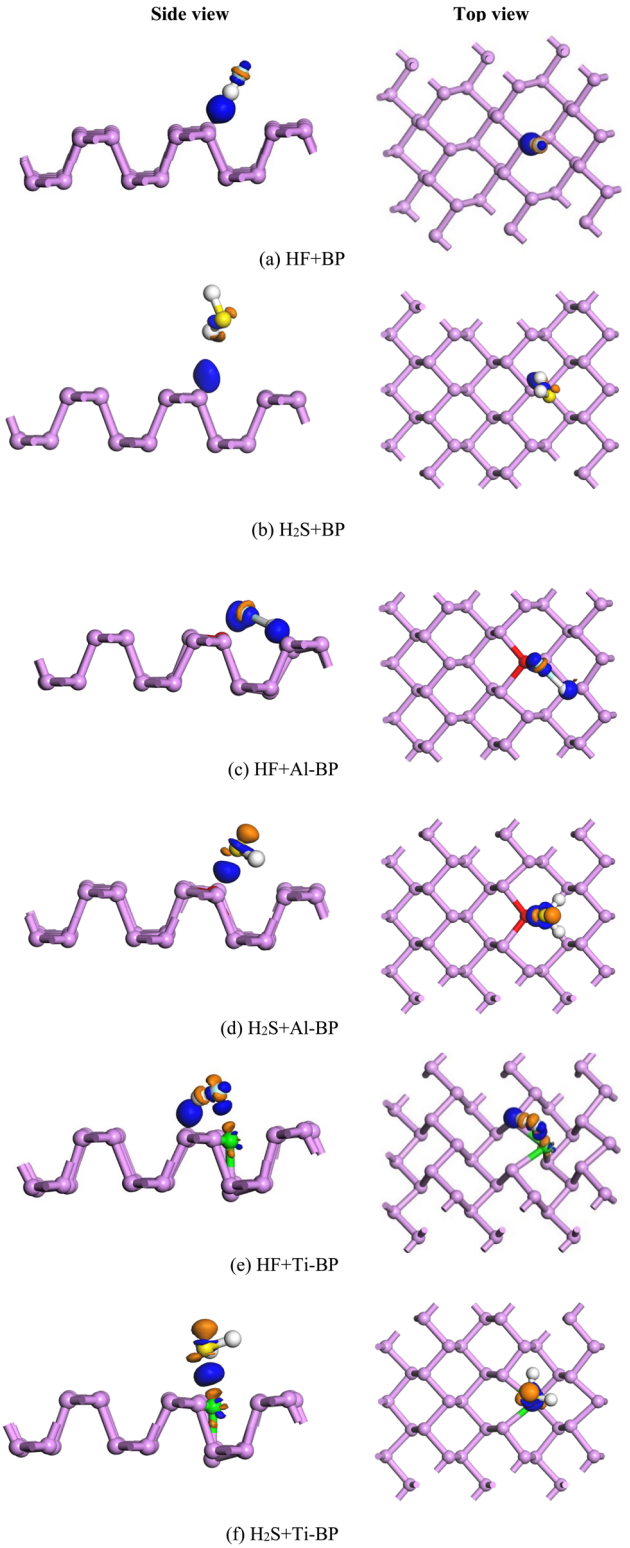

Fig. 4 Electron density difference map of (a) HF + BP, (b) H_2S + BP, (c) HF + Al-BP, (d) H_2S + Al-BP, (e) HF + Ti-BP, and (f) H_2S + Ti-BP. Orange and blue regions represent electron accumulation and depletion, respectively.

upon gas adsorption, with titanium's d-orbitals and high oxidation potential enhancing its activity as an adsorption site. During HF adsorption, Ti exhibits electron depletion while F accumulates charge, indicative of electrophilic interaction. Similar behavior is observed for H_2S, with electron accumulation near S and depletion at Ti reflecting active charge transfer.

Table 5 Comparison of band gap values for the adsorbent and adsorbent–gas complexes

Structure	Band gap (eV)
BP	0.877
HF + BP	0.879
H_2S + BP	0.866
Al-BP	0.783
HF + Al-BP	1.007
H_2S + Al-BP	0.991
Ti-BP	0.000
HF + Ti-BP	0.000
H_2S + Ti-BP	0.000

3.7 Band structure analysis

The band gap is defined as the energy interval between the valence band maximum (VBM) and the conduction band minimum (CBM).[65] The electronic band structure is a critical parameter for evaluating the sensing capability of adsorbent materials. Table 5 shows the band gap variations in BP and its modified structures upon interaction with HF and H_2S gas molecules. Fig. 5 also illustrates the changes in band gap of pristine and modified BP structures upon adsorption of HF and H_2S gas molecules. Our study finds that pristine BP exhibits semiconducting nature with a direct band gap of 0.877 eV, which aligns closely with previously reported values ranging from 0.80 to 0.91 eV.[66–68] This finding is also consistent with the experimentally measured transport band gap of 1.0–1.5 eV.[66,67,69] The close agreement with earlier first-principles studies highlights the reliability of our electronic structure calculations. Moreover, it confirms the suitability of the computational parameters adopted in this work. Upon adsorption of HF and H_2S gases, the band gap of pristine BP slightly increases to 0.879 eV and decreases to 0.866 eV, respectively, indicating minimal perturbation of its electronic structure. However, significant variations are observed in doped structures. Following Al doping, the band gap decreased, and both the valence and conduction bands shifted toward the Fermi level, indicating enhanced electronic activity. Specifically, upon HF gas adsorption on Al-BP, the CBM is located at the *M* *k*-point, whereas the VBM appears at the *Γ* *k*-point. We observed that after HF and H_2S adsorption on Al-BP, the band gap increases by approximately 28.6% and 26.5%, respectively, compared to the Al-BP band gap of 0.783 eV. This widening band gap suggests a moderate interaction between the nanosheets and gas molecules, which may influence the material's sensing performance. Moreover, Ti doping leads to the complete closure of the band gap (0.000 eV), suggesting a transition toward metallic behavior. In the case of both HF and H_2S gas adsorption, Ti-doped BP displays a zero-band gap, indicating strong electronic interactions and significant charge transfer between the adsorbent and the adsorbates.

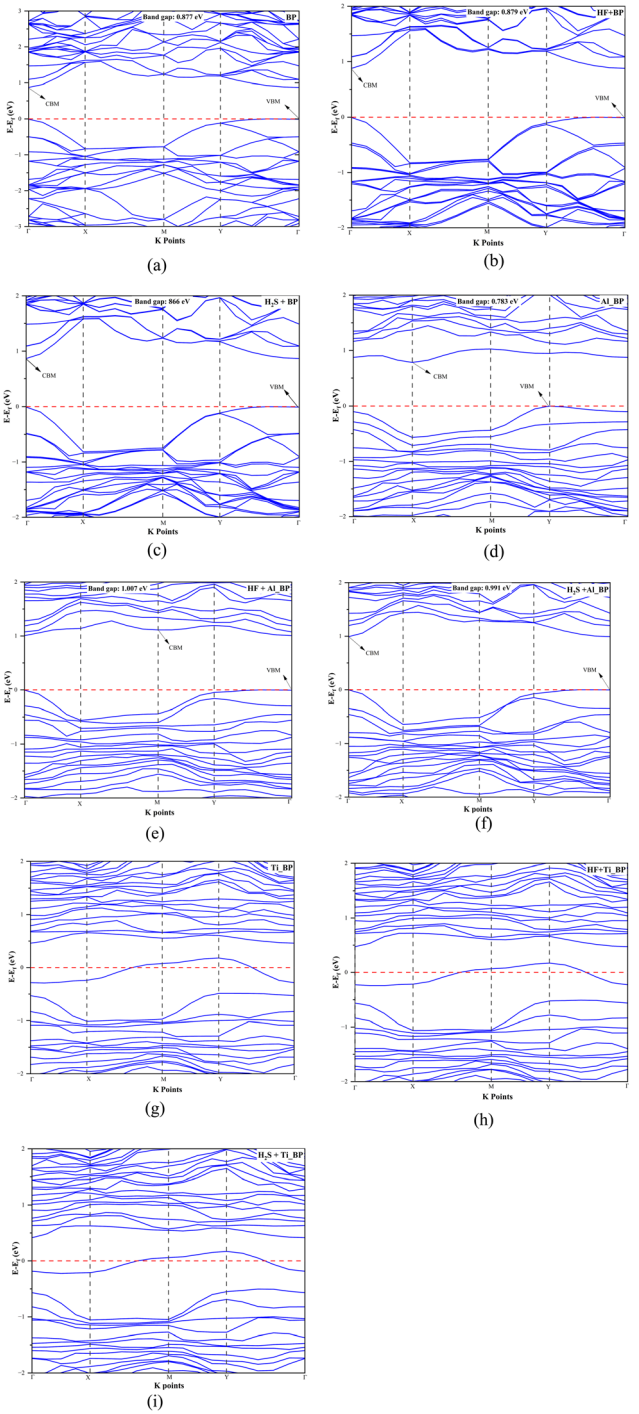

Fig. 5 Electronic band structures of pristine BP and its modified systems with gas adsorption: (a) pristine BP, (b) HF + BP, (c) H_2S + BP, (d) Al-BP, (e) HF + Al-BP, (f) H_2S + Al-BP, (g) Ti-BP, (h) HF + Ti-BP, and (i) H_2S + Ti-BP.

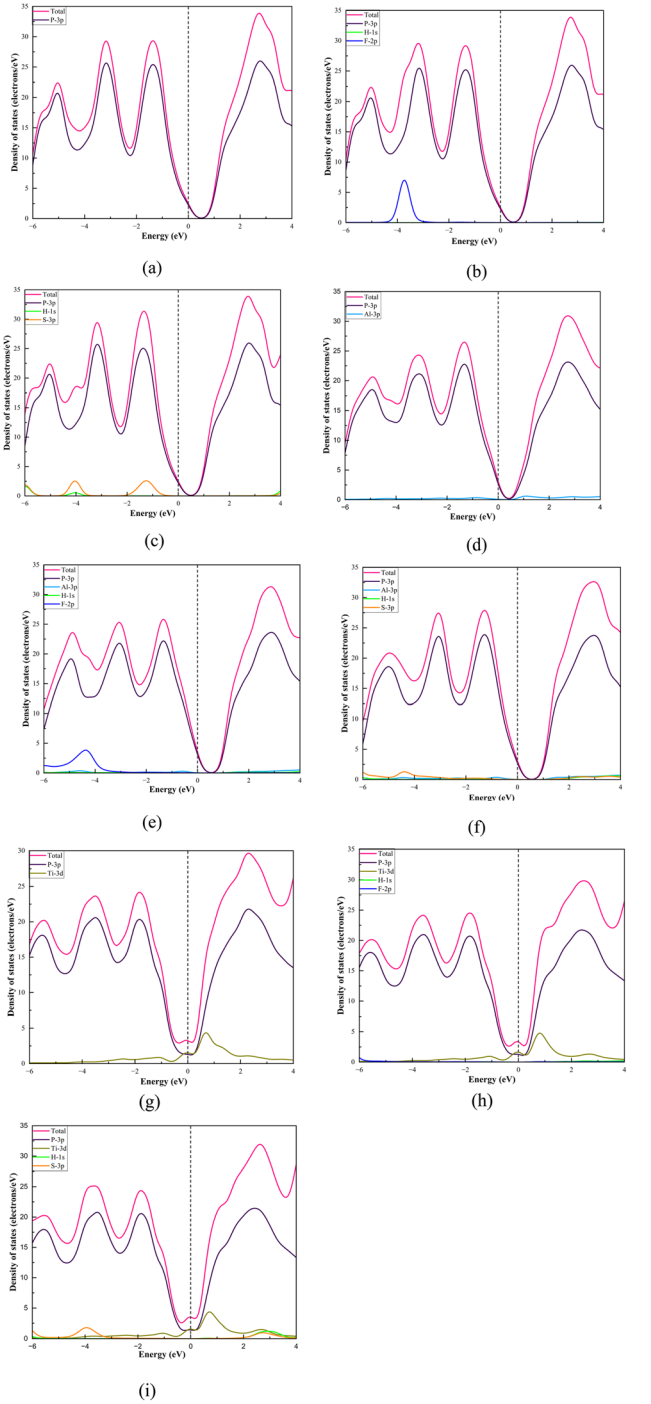

Fig. 6 Density of states (DOS) profiles for pristine and modified BP systems with gas adsorption: (a) pristine BP, (b) HF + BP, (c) H_2S + BP, (d) Al-BP, (e) HF + Al-BP, (f) H_2S + Al-BP, (g) Ti-BP, (h) HF + Ti-BP, and (i) H_2S + Ti-BP.

3.8 Density of states (DOS) analysis

The nature of a material (metallic or insulating) can be inferred by evaluating the density of states near the Fermi energy.[70] A non-zero density of states at the Fermi level indicates metallic conductivity due to the absence of a band gap, whereas a zero density of states with a band gap suggests semiconducting or insulating behavior.[71] This study analyzes the total and partial density of states (TDOS and PDOS) of pristine and metal-doped BP nanosheets to explain their electronic characteristics. Fig. 6 illustrates (TDOS and PDOS) for the optimized structures, highlighting the changes in electronic structure before and after the interaction. For pristine BP, the TDOS reveals a significant contribution from P-3p orbitals in both the valence band (VB)

and conduction band (CB), consistent with its known semiconducting nature.[72] The presence of a band gap near the Fermi level (E_F) confirms its semiconducting behavior. However, when BP is doped with elements such as Al or Ti, the electronic structure undergoes notable changes. For instance, in Al-doped BP, the Al-3p orbitals moderately contribute to the DOS, altering the original distribution of states. Similarly, in Ti-doped BP, the Ti-3d orbitals introduce new energy levels near the Fermi level, which eliminates the band gap, potentially leading to metallic behavior. The adsorption of gas molecules on doped BP further modulates the electronic properties. In the case of pristine BP, the P-3p orbital exhibited the most significant contribution in the valence and conduction bands upon interaction with HF and H_2S gases. For the BP–HF system, the PDOS analysis indicates negligible overlap between the P-3p, H-1s, and F-2p orbitals. Upon H_2S adsorption on the BP surface, the S-3p orbitals show a weak contribution to the electronic density of states in the energy range of −2 to 0 eV near E_F. The F-2p orbitals show the second-largest contribution to the VB in the energy range of −4 to 0 eV during HF adsorption on the Al-doped BP nanosheets. However, upon H_2S adsorption on Al-doped BP, the S-3p orbitals contribute equally to both the VB and CB. For the H_2S + Ti-BP complex, the Ti-3d orbitals mainly contribute to the CB within the range of 0 to 1 eV near E_F, with small contributions from the S-3p orbitals. For HF adsorption, the F-2p orbitals also play a significant role in influencing the electronic structure of the Ti-BP system. These interactions can lead to hybridization or charge transfer effects, which may further influence the conductive properties of the material.

3.9 Electrical conductivity and sensitivity analysis

The impact of the band gap on material behavior can be interpreted through its influence on electrical conductivity (σ), highlighting the associated physical mechanisms.[73] The relationship between electrical conductivity, bandgap, and temperature is represented by the following equation.[61]

$$\sigma = A \exp\left(\frac{-E_g}{2kT}\right) \quad (3)$$

Here, A is a constant term that remains undetermined due to the lack of experimental synthesis of the structures. Therefore, only the exponential term illustrates the variation of electrical conductivity as a function of the bandgap (E_g). In this case, the unit of σ is expressed as $A \times \Omega^{-1}\ m^{-1}$. Table 6 summarizes the computed electrical conductivity values for the studied structures. In this research, we observed that electrical conductivity increases exponentially as the bandgap decreases and also rises with increasing temperature from 300 K to 500 K. For pristine BP, the calculated conductivity is $4.28 \times 10^{-8} A \times \Omega^{-1}\ m^{-1}$. Due to HF adsorption, the conductivity decreased by approximately 3.97%, whereas for H_2S gas, it increased by around 24.77% compared to pristine BP at 300 K. Conversely, the conductivity decreased upon adsorption of both HF and H_2S on the Al-BP complex compared to that of pristine Al-BP. Ti doping in BP leads to a zero bandgap, resulting in maximum conductivity by enabling free electron movement and improved charge transport. Such changes in electrical conductivity enable the gas sensor to detect gas molecules when they adsorb on the sensor surface.[52]

To understand the interaction mechanism, we computed the sensitivity of the studied complexes over the temperature range of 300–500 K. The sensitivity of an adsorbent to specific gas molecules can be quantified by comparing its conductivity before and after gas adsorption, as follows:[74]

$$\text{Sensitivity} = \frac{\left|\sigma_{\text{adsorbent}} - \sigma_{\text{adsorbent+gas}}\right|}{\sigma_{\text{adsorbent}}} \times 100\% \quad (4)$$

where $\sigma_{\text{adsorbent}}$ and $\sigma_{\text{adsorbent+gas}}$ represent the electrical conductivities of the pure adsorbent and the adsorbent after gas adsorption respectively. We observed differences in sensitivity

Table 7 Sensitivity of various gas–adsorbed structures at different temperatures (300 K, 400 K, and 500 K)

	Sensitivity		
Structure	300 K	400 K	500 K
HF + BP	0.04	0.03	0.02
H_2S + BP	0.25	0.17	0.14
HF + Al-BP	0.98	0.96	0.93
H_2S + Al-BP	0.97	0.95	0.91
HF + Ti-BP	—	—	—
H_2S + Ti-BP	—	—	—

Table 6 Calculated bandgap (E_g), Fermi energy (E_F), work function (Φ), and electrical conductivity (σ) for adsorbent and gas–adsorbent complexes

					σ ($A \times \Omega^{-1}\ m^{-1}$)		
Structure	E_g (eV)	E_F (eV)	Φ (eV)	$\Delta\Phi$ (eV)	300 K	400 K	500 K
BP	0.877	−1.845	1.8452	—	4.28×10^{-8}	2.98×10^{-6}	3.78×10^{-5}
HF + BP	0.879	−1.719	1.7194	0.126	4.11×10^{-8}	2.89×10^{-6}	3.7×10^{-5}
H_2S + BP	0.866	−1.750	1.7509	0.094	5.34×10^{-8}	3.50×10^{-6}	4.32×10^{-5}
Al-BP	0.783	−1.802	1.8022	—	2.66×10^{-7}	1.17×10^{-5}	1.13×10^{-4}
HF + Al-BP	1.007	−1.576	1.5761	0.226	3.46×10^{-9}	4.53×10^{-7}	8.43×10^{-6}
H_2S + Al-BP	0.991	−1.402	1.4023	0.399	4.72×10^{-9}	5.79×10^{-7}	1.01×10^{-5}
Ti-BP	0.000	−1.743	1.7437	—	—	—	—
HF + Ti-BP	0.000	−1.643	1.6434	0.100	—	—	—
H_2S + Ti-BP	0.000	−1.579	1.5793	0.164	—	—	—

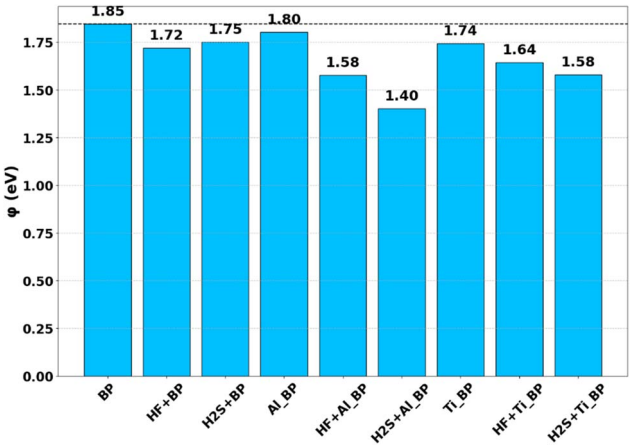

Fig. 7 Variation in work function of the studied structures before and after gas adsorption.

among BP, Al-BP, and Ti-BP toward HF and H_2S gas molecules at varying temperatures, as shown in Table 7. We observed a consistent decrease in sensitivity with increasing temperature across all investigated structures, which can be attributed to the reduced adsorption of gas molecules at elevated temperatures. Among all the gas adsorption structures, Al-BP exhibits the highest sensitivity to the HF gas molecule at 300 K. As the temperature rises from 300 K to 500 K, the sensitivity reduces by approximately 2.04% at 400 K and by 5.10% at 500 K. On the other hand, BP is the least sensitive to HF, and its sensitivity gradually decreases with increasing temperature. For the pristine systems, the H_2S + BP configuration demonstrated higher sensitivity than HF + BP at all investigated temperatures. Furthermore, Al-BP shows the second greatest sensitivity toward H_2S compared to the other structures. These findings demonstrate that Al-doped BP exhibits significantly enhanced sensitivity toward HF and H_2S gas molecules compared to pristine BP. In the case of the Ti-BP, it possesses a high and stable

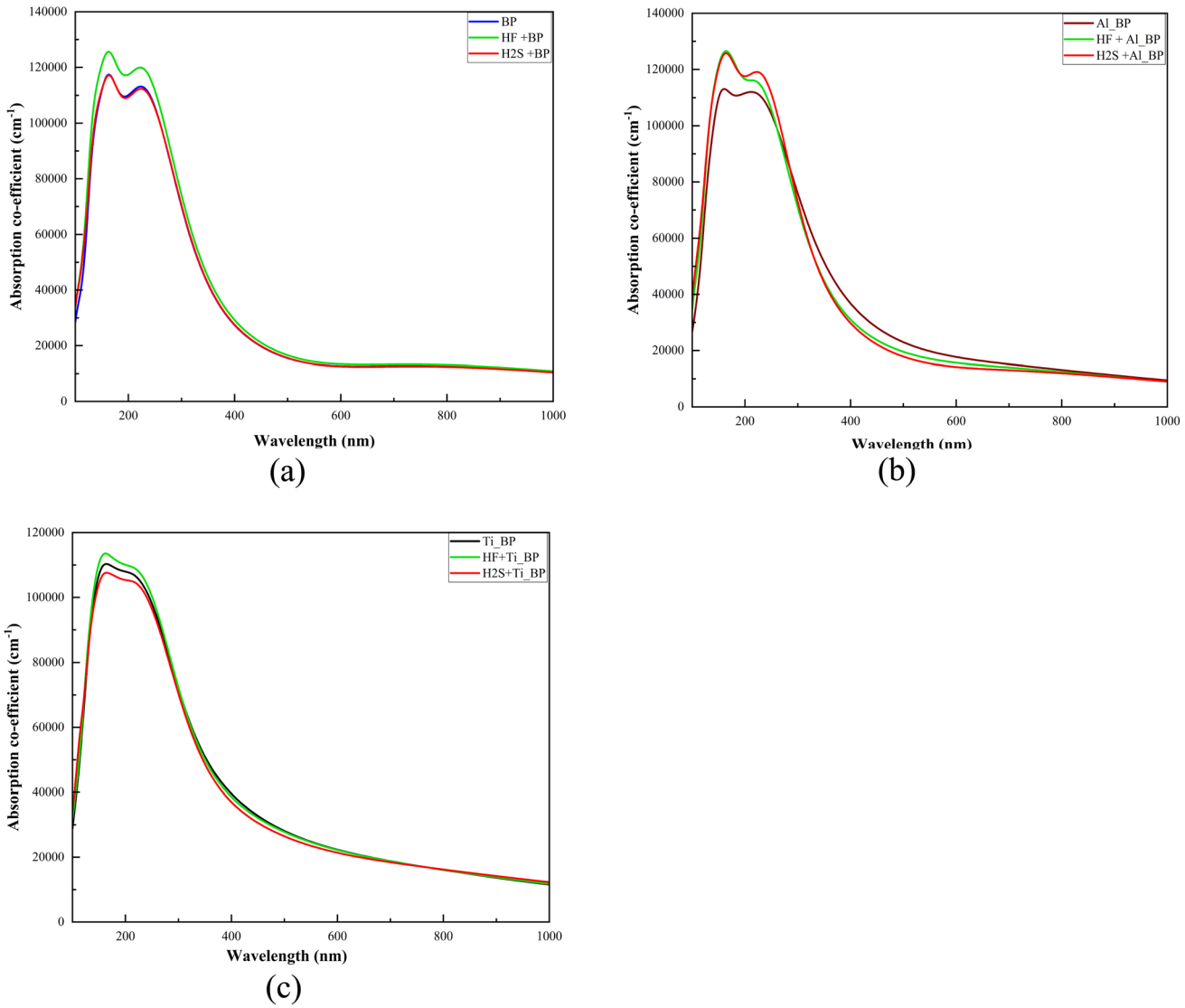

Fig. 8 Adsorption coefficient of (a) pristine BP, (b) Al-BP, and (c) Ti-BP with HF and H_2S gas molecules.

density of free charge carriers due to its zero band gap.[75] When a gas molecule is adsorbed onto its surface, the resulting charge transfer is typically negligible compared to the bulk carrier density. Consequently, the sensitivity of such a conductive system to gas molecules is almost undetectable.[76]

3.10 Work function

The work function (Φ) refers to the minimum energy required to transfer an electron from the Fermi level of a material to a point just outside its surface, known as the vacuum level.[77] It is evaluated according to the following expression,[78]

$$\Phi = |V_\infty - E_F| \quad (5)$$

The term V_∞ represents the vacuum potential at an infinite distance from the surface of the adsorbent, where the potential is assumed to be zero.[52] Here, E_F is the Fermi energy. Table 6 summarizes the calculated values of work function for the studied configurations. The effect of HF and H_2S gas adsorption on the work function of pristine and modified BP is illustrated in Fig. 7. In all cases, we observed that the work function values decreased due to gas adsorption, indicating charge transfer between the adsorbents and adsorbates. The pristine BP exhibited a baseline work function of 1.8452 eV, which decreased by approximately 6.81% and 5.12% upon adsorption of HF and H_2S molecules, respectively. Among the gas–adsorbed systems studied, the H_2S + Al-BP system showed the lowest work function (1.4023 eV), suggesting enhanced electron emission. Conversely, the H_2S + BP configuration presented the maximum work function of 1.7509 eV, indicating reduced electron emission and making it suitable for use as a protective material. For Al-doped BP, a notable reduction in work function

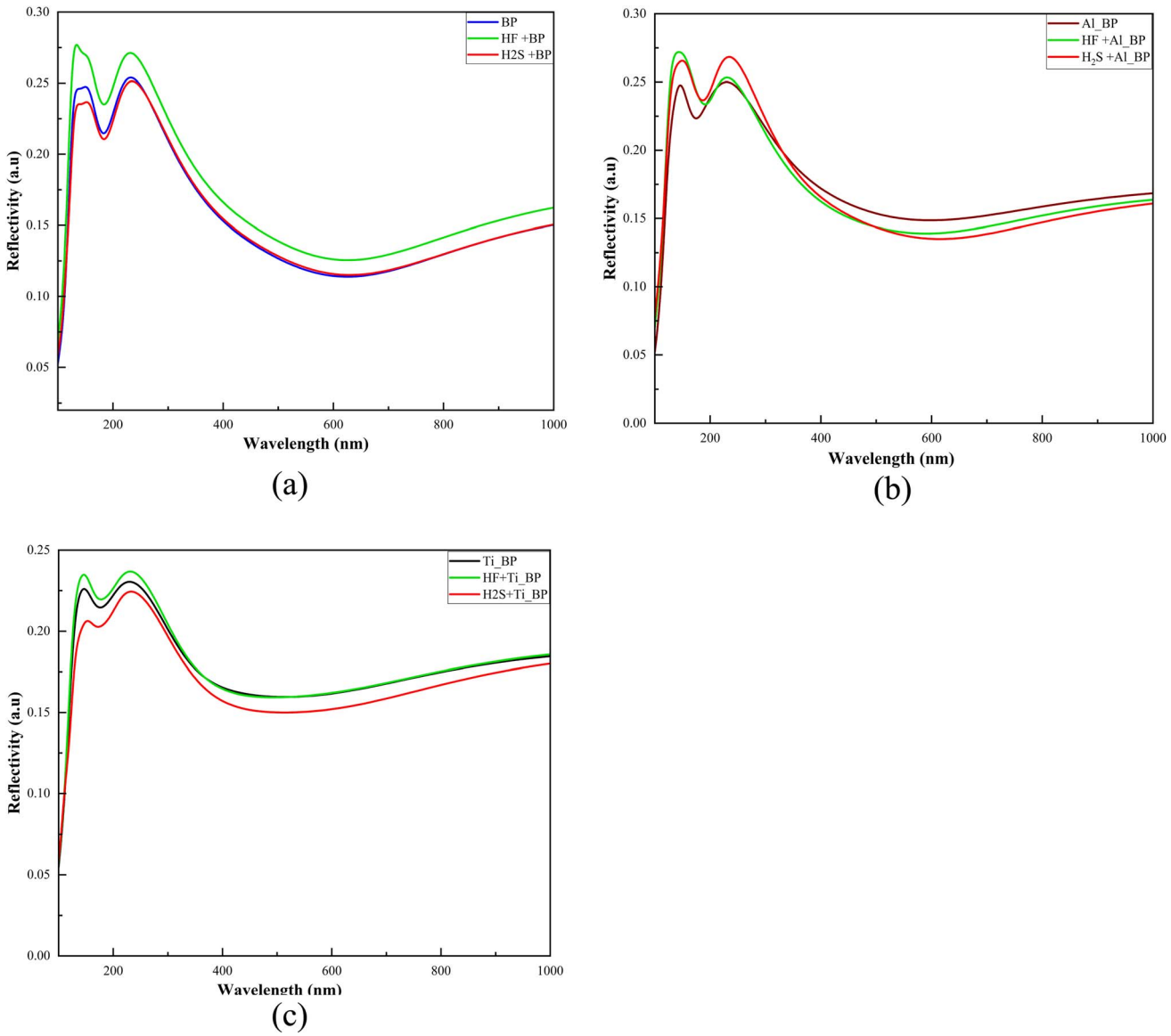

Fig. 9 Reflectivity of (a) pristine BP, (b) Al-BP, and (c) Ti-BP with HF and H_2S gas molecules.

was observed, with decreases of approximately 12.57% and 22.16% upon HF and H_2S adsorption, respectively. These reductions correspond to $\Delta\Phi$ values of 0.226 eV and 0.399 eV, respectively, highlighting the enhanced interaction between Al-BP and the adsorbed gas molecules. We also observed a moderate variation in work function during HF and H_2S adsorption on Ti-BP, with reductions of approximately 5.72% and 9.47%, respectively. These findings indicate stronger electronic interactions and improved sensing capabilities of the doped systems compared to pristine BP. Gas adsorption induces a significant change in the work function, which can be experimentally measured by the Kelvin method to develop work function-based sensors.[79] The Richardson–Dushman relation mathematically characterizes the dependence of conductivity changes on the work function as follows,[80]

$$J_R = B_R T^2 e^{-\frac{\Phi}{k_B T}} \quad (6)$$

where B_R is the Richardson constant, and J_R represents the density of emitted charge carriers. This equation reveals that the emission of charge carriers from the material increases exponentially as the work function Φ decreases, highlighting the strong sensitivity of carrier emission to changes in Φ.

3.11 Optical properties analysis

The optical properties of a material fundamentally govern its interaction with electromagnetic radiation across various wavelengths, influencing phenomena such as absorption, reflection, refraction, and transmission.[81] In this study, the optical properties of pristine and Al and Ti-doped BP nanosheets—including absorption, reflectivity, and optical conductivity—were investigated to understand their interactions with light. The results are summarized in Fig. 8, 9, and 10, respectively. Pristine BP exhibits strong absorption in the ultraviolet (UV) region, with peak absorption observed at shorter

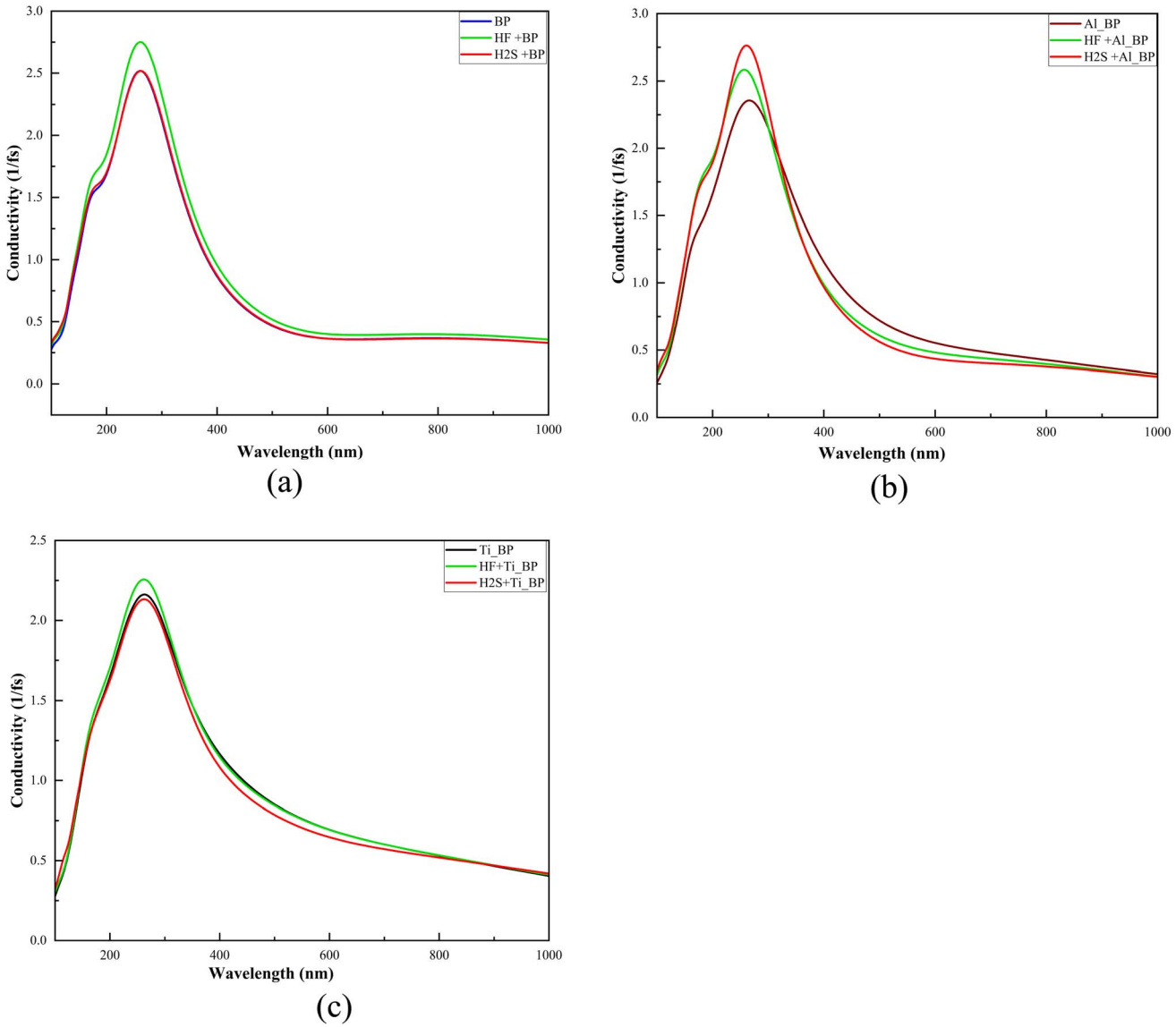

Fig. 10 Conductivity of (a) pristine BP, (b) Al-BP, and (c) Ti-BP with HF and H_2S gas molecules.

wavelengths (~200 nm). Upon adsorption of HF and H_2S, the absorption spectra of BP show minimal shifts, indicating limited interaction between the gas molecules and the pristine structure. For Ti-doped BP, the absorption edge shifts slightly toward longer wavelengths after gas adsorption, indicating a redshift induced by doping and gas interactions. Al-doped BP also exhibits a more pronounced redshift, especially upon H_2S adsorption, with the absorption edge extending to 200–300 nm. This significant shift suggests stronger electronic coupling between H_2S molecules and Al-doped BP nanosheets.

The reflectivity spectra show that pristine BP reflects only a small fraction of incident light in the UV range, with negligible changes observed after adsorption of HF and H_2S gas molecules. However, Ti-BP and Al-BP exhibit altered reflectivity patterns upon gas exposure. Upon H_2S adsorption, Ti-doped BP exhibits a slight increase in reflectivity in the UV range near 250 nm, while Al-doped BP shows a more pronounced rise, with reflectivity peaking around 300 nm. This suggests that Al-doped BP undergoes significant surface electronic modifications upon gas interaction, resulting in increased reflectivity at longer wavelengths. Similarly, after HF adsorption, Al-doped BP exhibits a modest increase in reflectivity near 200 nm, while Ti-doped BP shows a more substantial enhancement, with reflectivity peaking close to 300 nm.

Pristine BP exhibits high optical conductivity in the UV region, consistent with its strong absorption characteristics. Adsorption of HF and H_2S does not significantly alter this trend. In contrast, Al and Ti-doped BP exhibit enhanced optical conductivity from the UV to the near-visible region following gas adsorption. In the Al-doped BP + H_2S complex, optical conductivity increases significantly, correlating with the observed redshift in absorption, whereas HF adsorption leads to a noticeable decrease in conductivity. For Ti-doped BP, HF adsorption leads to a notable enhancement in optical conductivity, indicating increased charge carrier activity.[81] Finally, the optical properties of BP are significantly influenced by doping with Ti and Al, as well as by adsorption of HF and H_2S gases. These modifications highlight the potential of doped BP nanosheets for selective gas-sensing applications.

3.12 RDG analysis

Reduced Density Gradient (RDG) method provides a spatially resolved and visual analysis of non-covalent interactions within a molecular system by examining the electron density and its derivatives.[82] It is mathematically expressed as:

$$\mathrm{RDG}(r) = c\frac{|\nabla\rho(r)|}{\rho(r)^{4/3}} \quad (7)$$

where $\rho(r)$ represents the electron density at a given position r, $\nabla\rho(r)$ denotes its gradient, and c is a proportionality constant.[82] Fig. 11 presents the scatterplot and isosurface plot of RDG for pristine and doped BP interacting with toxic gas molecules. The scatterplot displays the RDG on the vertical axis, while the horizontal axis represents the electron density multiplied by the sign of the second Hessian eigenvalue, $\mathrm{sign}(\lambda_2)\rho$. Regions of low

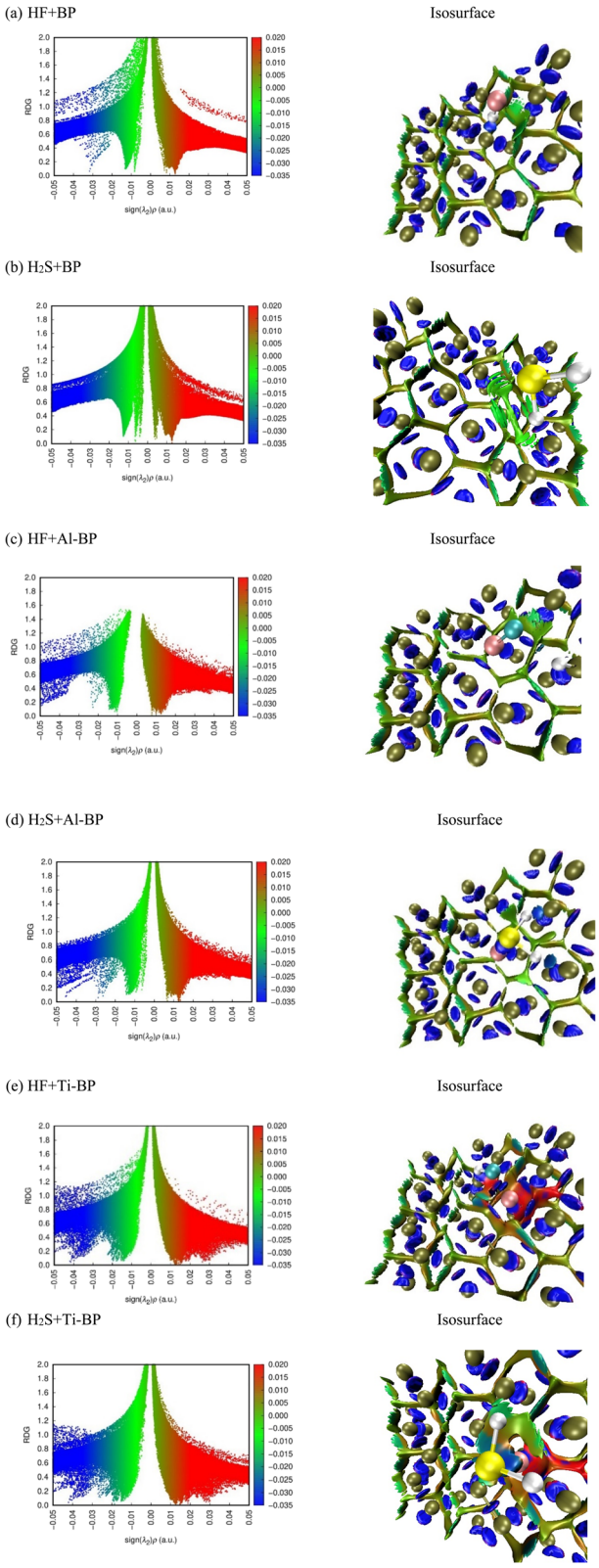

Fig. 11 Visualization of reduced density gradient (RDG) isosurfaces and corresponding scatter plots of (a) HF + BP, (b) H_2S + BP, (c) HF + Al-BP, (d) H_2S + Al-BP, (e) HF + Ti-BP, and (f) H_2S + Ti-BP.

Table 8 Comparative analysis of HF and H_2S gas sensing performance of various 2D nanomaterials, based on key parameters including adsorption energy (E_{ads}), band gap (E_g), charge transfer (Δq), work function (Φ), and recovery time

Structure	Gas	E_{ads} (eV)	E_g (eV)	Δq (e)	Φ (eV)	Recovery time (s)	Ref.
BP	HF	−0.276	0.879	−0.08	1.719	5.7×10^{-11}	—
BP	H_2S	−0.133	0.866	0.00	1.751	2.3×10^{-13}	—
Al-BP	HF	−1.651	1.007	−0.62	1.576	6.7×10^{12}	—
Al-BP	H_2S	−0.828	0.991	0.09	1.402	1.1×10^{-1}	—
Ti-BP	HF	−0.502	0.000	−0.06	1.643	3.5×10^{-7}	—
Ti-BP	H_2S	−0.584	0.000	0.08	1.579	8.5×10^{-6}	—
$PdAs_2$	HF	−0.390	0.300	0.11	4.708	4.2×10^{-6}	85
$PdAs_2$	H_2S	−0.490	0.280	−0.13	4.573	1.8×10^{-4}	85
ZnS ML	HF	−0.860	2.940	−0.08	6.402	2.8×10^{2}	86
β-TeO_2	H_2S	−0.298	2.705	0.003	—	1.0×10^{-7}	87
GeS_2	HF	−0.250	0.930	−0.13	—	1.5×10^{-8}	88
GeS_2	H_2S	−0.230	0.440	−0.02	—	6.5×10^{-9}	88
CuBr	HF	−0.222	3.191	−0.03	5.130	7.1×10^{-9}	89
BNNS	H_2S	−0.175	4.035	−0.02	4.230	9.0×10^{-10}	90
Pristine twin graphene	HF	−0.160	0.710	−0.05	—	—	91
Pristine twin graphene	H_2S	−0.220	0.680	−0.06	—	—	91

electron density indicate weak van der Waals interactions, whereas high-density regions correspond to stronger non-covalent forces, characterized by sharp density gradients and significant electronic interactions.[55,83] The value of the sign(λ_2)ρ allows for a better interpretation of the behavior of the interactions. Specifically, a positive sign(λ_2)ρ value (>0) denotes repulsive interactions, while a negative value (<0) corresponds to attractive interactions. Values of sign(λ_2)ρ approaching zero ($\approx$0) are indicative of weak interactions.[84] As illustrated in Fig. 11, the sign(λ_2)ρ values span from −0.035 to 0.020 a.u. and are visualized through a color scale comprising blue, green, and red regions. In the interaction of pristine BP with HF and H_2S, the RDG isosurfaces appear predominantly green, corresponding to low values of the second eigenvalue of the electron density Hessian ($\lambda_2 \approx 0$), which indicates weak van der Waals interactions. These findings indicate that the interaction is dominated by physisorption with negligible charge transfer. Upon Al doping, blue isosurfaces emerge prominently between HF and Al sites ($\lambda_2 < 0$), revealing attractive interactions such as hydrogen bonding. The adsorption of H_2S on Al-BP exhibits significantly enhanced interaction regions, evidenced by more intense blue-green isosurfaces (λ_2 values typically from −0.03 to −0.04 a.u.) compared to pristine BP. This enhancement suggests a stronger binding affinity, likely arising from orbital hybridization or electron donation facilitated by Al doping. In the HF + Ti-BP configuration, the RDG isosurfaces exhibit increased intensity and spatial expansion across a broader region of the BP surface. Moreover, the isosurfaces display more pronounced blue spikes, reflecting stronger attractive interactions, with λ_2 values clustering near −0.04 a.u. In H_2S + Ti-BP, we observed blue and green spikes, which indicate the presence of strong attractive and van der Waals interactions.

3.13 Comparison summary

Table 8 presents a comparison of the HF and H_2S gas sensing performance of various 2D structures.

4. Conclusion

In this work, we used DFT method to design and optimize BP, Al-BP, and Ti-BP structures for the effective adsorption of HF and H_2S gas molecules. Molecular dynamics simulations demonstrate the thermodynamic stability of all studied adsorbents at room temperature. The adsorption energies of BP are relatively low, indicating weak physisorption of these gas molecules. In contrast, doping with Al and Ti significantly enhances the adsorption performance. Notably, the HF + Al-BP system exhibits the highest adsorption energy (−1.6506 eV), suggesting strong chemisorption. On the other hand, Ti-BP shows physisorption (stronger than pristine BP) and non-covalent interaction with the adsorbates. Ti-doped BP exhibits a faster recovery time, whereas Al-doped BP shows a comparatively higher recovery time due to stronger gas–sheet interaction. Semiconductor-to-metal transition observed due to Ti-doping on BP. The change in work function further confirms gas adsorption, while sensitivity analysis reveals that doped BP exhibits a stronger response to the gas than pristine BP. The optical properties exhibit a notable red shift in the UV region upon interaction with gas molecules, suggesting that it is another parameter for gas adsorption confirmation. According to RDG analysis, HF and H_2S interact with the doped systems *via* hydrogen bonding and van der Waals interactions, respectively. Therefore, these enhancements suggest that Al and Ti-doped BP possess significant potential for the selective detection of toxic gases, compared to its pristine form.

Author contributions

Rashek Dewan Daymond: data curation, formal analysis, investigation, visualization, writing – original draft, Fatin Hasnat Shihab: data curation, formal analysis, visualization, writing – original draft, Nihal Siddique: data curation, validation, writing – review & editing, Mohammad Tanvir Ahmed: formal analysis, project administration, validation, writing –

review & editing, Abdullah Al Roman: resources, software, validation, writing – review & editing, Debashis Roy: conceptualization, methodology, project administration, supervision, writing – review & editing.

Conflicts of interest

The authors declare that there are no conflicts of interest regarding the publication of this paper.

Data availability

The datasets generated during and/or analysed during the current study (including simulation unit cell to design the 2D black phosphorus) are not publicly available as further research is ongoing, but they are available from the authors upon reasonable request.

References

1 V. Kumar, K. Rajput and D. R. Roy, Sensing applications of GeBi nanosheet for environmentally toxic/non-toxic gases: Insights from density functional theory calculations, *Appl. Surf. Sci.*, 2022, **606**, 154741.
2 I. J. Tonny, M. Khatun, D. Roy, A. Al Roman and M. T. Ahmed, A first-principles investigation of BF_3 and ClF_3 gas sensing on N-defected AlN nanosheets, *AIP Adv.*, 2024, **14**, 045136.
3 F. Momen, F. Shayeganfar and A. Ramazani, Boron-rich hybrid BCN nanoribbons for highly ambient uptake of H_2S, HF, NH_3, CO, CO_2 toxic gases, *Phys. Chem. Chem. Phys.*, 2024, **26**, 5262–5288.
4 R. Majidi and A. Ramazani, Detection of HF and H_2S with pristine and Ti-embedded twin graphene: A density functional theory study, *J. Phys. Chem. Solids*, 2019, **132**, 31–37.
5 B. A. Kalwar, W. Fangzong, A. M. Soomro, M. R. Naich, M. H. Saeed and I. Ahmed, Highly sensitive work function type room temperature gas sensor based on Ti doped hBN monolayer for sensing CO_2, CO, H_2S, HF and NO. A DFT study, *RSC Adv.*, 2022, **12**, 34185–34199.
6 X. Zhang, Z. Dai, Q. Chen and J. Tang, A DFT study of SO_2 and H_2S gas adsorption on Au-doped single-walled carbon nanotubes, *Phys. Scr.*, 2014, **89**, 065803.
7 Y. Zhou, Z. Hu, H. Zhao, Y. Wang, J. Li and C. Zou, Two-dimensional black phosphorus/tin oxide heterojunctions for high-performance chemiresistive H_2S sensing, *Anal. Chim. Acta*, 2023, **1245**, 340825.
8 S. A. Adalikwu, H. Louis, H. O. Edet, I. Benjamin, T. G. C. Egemonye, E. A. Eno and A. S. Adeyinka, Detection of hydrogen fluoride (HF) gas by $Mg_{12}O_{11}$-X (X = S, P, N, and B) nanosurfaces, *Chem. Phys. Impact*, 2022, **5**, 100129.
9 R. Torres-Sánchez, D. Sánchez-Rodas, A. M. Sánchez de la Campa and J. D. de la Rosa, Hydrogen fluoride concentrations in ambient air of an urban area based on the emissions of a major phosphogypsum deposit (SW, Europe), *Sci. Total Environ.*, 2020, **714**, 136891.
10 A. A. Ramanathan, Defect Functionalization of MoS_2 nanostructures as toxic gas sensors: A review, *IOP Conf. Ser.: Mater. Sci. Eng.*, 2018, **305**, 012001.
11 F. J. Godínez-García, R. Guerrero-Rivera, J. A. Martínez-Rivera, E. Gamero-Inda and J. Ortiz-Medina, Advances in two-dimensional engineered nanomaterials applications for the agro- and food-industries, *J. Sci. Food Agric.*, 2023, **103**, 5201–5212.
12 H. Tang, L. N. Sacco, S. Vollebregt, H. Ye, X. Fan and G. Zhang, Recent advances in 2D/nanostructured metal sulfide-based gas sensors: mechanisms, applications, and perspectives, *J. Mater. Chem. A*, 2020, **8**, 24943–24976.
13 Q. Lu, Y. Yu, Q. Ma, B. Chen and H. Zhang, 2D Transition-Metal-Dichalcogenide-Nanosheet-Based Composites for Photocatalytic and Electrocatalytic Hydrogen Evolution Reactions, *Adv. Mater.*, 2016, **28**, 1917–1933.
14 S. Tongay, Preface to a Special Topic: 2D Materials and Applications, *Appl. Phys. Rev.*, 2018, **5**, 1–3.
15 X. Zhuang, Y. Mai, D. Wu, F. Zhang and X. Feng, Two-Dimensional Soft Nanomaterials: A Fascinating World of Materials, *Adv. Mater.*, 2015, **27**, 403–427.
16 K. S. Novoselov, A. K. Geim, S. V. Morozov, D. Jiang, Y. Zhang, S. V. Dubonos, I. V. Grigorieva and A. A. Firsov, Electric field in atomically thin carbon films, *Science*, 2004, **306**, 666–669.
17 V. Van Cat, N. X. Dinh, V. Ngoc Phan, A. T. Le, M. H. Nam, V. Dinh Lam, T. Van Dang and N. Van Quy, Realization of graphene oxide nanosheets as a potential mass-type gas sensor for detecting NO_2, SO_2, CO, and NH_3, *Mater. Today Commun.*, 2020, **25**, 101682.
18 Y. Seekaew and C. Wongchoosuk, A novel graphene-based electroluminescent gas sensor for carbon dioxide detection, *Appl. Surf. Sci.*, 2019, **479**, 525–531.
19 S. U. D. Shamim, D. Roy, S. Alam, A. A. Piya, M. S. Rahman, M. K. Hossain and F. Ahmed, Doubly doped graphene as gas sensing materials for oxygen-containing gas molecules: A first-principles investigation, *Appl. Surf. Sci.*, 2022, **596**, 153603.
20 M. Lalitha, Y. Nataraj and S. Lakshmipathi, Calcium decorated and doped phosphorene for gas adsorption, *Appl. Surf. Sci.*, 2016, **377**, 311–323.
21 L. Qin, S. Jiang, H. He, G. Ling and P. Zhang, Functional black phosphorus nanosheets for cancer therapy, *J. Controlled Release*, 2020, **318**, 50–66.
22 S. Bagheri, N. Mansouri and E. Aghaie, Phosphorene: A new competitor for graphene, *Int. J. Hydrogen Energy*, 2016, **41**, 4085–4095.
23 G. Lee, S. Kim, S. Jung, S. Jang and J. Kim, Suspended black phosphorus nanosheet gas sensors, *Sens. Actuators, B*, 2017, **250**, 569–573.
24 W. Cao, D. Lai, J. Yang, L. Liu, H. Wu, J. Wang and Y. Liu, Research Progress on the Preparation Methods for and Flame Retardant Mechanism of Black Phosphorus and Black Phosphorus Nanosheets, *Nanomaterials*, 2024, **14**, 892.
25 H. Liu, Y. Du, Y. Deng and P. D. Ye, Semiconducting black phosphorus: Synthesis, transport properties and electronic applications, *Chem. Soc. Rev.*, 2015, **44**, 2732–2743.

26 X. Ling, H. Wang, S. Huang, F. Xia and M. S. Dresselhaus, The renaissance of black phosphorus, *Proc. Natl. Acad. Sci. U. S. A.*, 2015, **112**, 4523–4530.
27 Y. Zhang, Q. Jiang, P. Lang, N. Yuan and J. Tang, Fabrication and applications of 2D black phosphorus in catalyst, sensing and electrochemical energy storage, *J. Alloys Compd.*, 2021, **850**, 156580.
28 D. R. Roy, M. A. Zaeem, S. Thomas and V. Kumar, Two-dimensional boron–phosphorus monolayer for reversible NO_2 gas sensing, *ACS Appl. Nano Mater.*, 2020, **3**, 10073–10081.
29 M. Lalitha, Y. Nataraj and S. Lakshmipathi, Calcium decorated and doped phosphorene for gas adsorption, *Appl. Surf. Sci.*, 2016, **377**, 311–323.
30 S. J. Ray, First-principles study of MoS_2, phosphorene and graphene based single electron transistor for gas sensing applications, *Sens. Actuators, B*, 2016, **222**, 492–498.
31 S. Y. Cho, Y. Lee, H. J. Koh, H. Jung, J. S. Kim, H. W. Yoo, J. Kim and H. T. Jung, Superior Chemical Sensing Performance of Black Phosphorus: Comparison with MoS_2 and Graphene, *Adv. Mater.*, 2016, **28**, 7020–7028.
32 L. Kou, T. Frauenheim and C. Chen, Phosphorene as a superior gas sensor: Selective adsorption and distinct i–V response, *J. Phys. Chem. Lett.*, 2014, **5**, 2675–2681.
33 M. Ghambarian, Z. Azizi and M. Ghashghaee, Hydrogen detection on black phosphorene doped with Ni, Pd, and Pt: Periodic density functional calculations, *Int. J. Hydrogen Energy*, 2020, **45**, 16298–16309.
34 M. Ubaid, A. Aziz and B. S. Pujari, Indium doped phosphorene as a potential gas sensor: a study using density functional theory, *Electron. Struct.*, 2020, **2**, 035001.
35 A. Ebrahimi and M. Izadyar, Li-decorated black phosphorene: A promising platform for gas molecule adsorption, *Int. J. Quantum Chem.*, 2024, **124**, e27427.
36 D. Talukdar, D. Mohanta and G. A. Ahmed, Nitrogen doped compound defect in black phosphorene for enhanced gas sensing, *Surf. Interfaces*, 2024, **51**, 104699.
37 Z. Chen, R. Li, X. Peng, H. Jiang and H. Zeng, Exploring adsorption and sensing mechanism of Li-decorated N-doped black phosphorene for toxic gases: Insights from first-principles calculations, *Surf. Interfaces*, 2024, **52**, 104872.
38 L. Yang, T. Wang, T. Xu and X. Li, *The Small Gas Molecule Sensing Properties of the Au-Doped Stable Black Arsenic Phosphorus Monolayer*, 2024, p. 18.
39 J. J. Li, X. Qi, F. Xie, D. Wu, Z. Q. Fan and X. Q. Cui, Methane gas adsorption and detection using the metal-decorated blue phosphorene, *Appl. Surf. Sci.*, 2022, **596**, 153511.
40 X. Duan, D. Xu, W. Jia, B. Sun, R. Li, R. Yan and W. Zhao, Pt and black phosphorus co-modified flower-like WS_2 composites for fast NO_2 gas detection at low temperature, *Nanoscale*, 2024, **16**, 2478–2489.
41 M. V. Balaji, V. Nagarajan and R. Chandiramouli, Aldehyde adsorption studies on α-arsenic phosphorus monolayer – A first-principles investigation, *Comput. Theor. Chem.*, 2025, **1248**, 115162.
42 M. D. Segall, P. J. D. Lindan, M. J. Probert, C. J. Pickard, P. J. Hasnip, S. J. Clark and M. C. Payne, First-principles simulation: ideas, illustrations and the CASTEP code, *J. Phys.: Condens. Matter*, 2002, **14**, 2717.
43 J. P. Perdew, Generalized gradient approximations for exchange and correlation: A look backward and forward, *Phys. B*, 1991, **172**, 1–6.
44 R. González-González, M. G. Salas-Zepeda and A. Tlahuice-Flores, New two-dimensional carbon nitride allotrope with 1 : 1 stoichiometry featuring spine-like structures: a structural and electronic DFT-D study, *Phys. Chem. Chem. Phys.*, 2019, **21**, 15282–15285.
45 A. M. Ali, M. Y. Kwaya, A. Mijinyawa, A. A. Aminu and Z. M. Usman, Molecular dynamics and energy distribution of methane gas adsorption in shales, *J. Nat. Gas Geosci.*, 2023, **8**, 1–15.
46 T. Lu and F. Chen, Multiwfn: A multifunctional wavefunction analyzer, *J. Comput. Chem.*, 2012, **33**, 580–592.
47 T. Lu, A comprehensive electron wavefunction analysis toolbox for chemists, Multiwfn, *J. Chem. Phys.*, 2024, **161**, 082503.
48 M. Mohammadzaheri, S. Jamehbozorgi, M. D. Ganji, M. Rezvani and Z. Javanshir, Toward functionalization of ZnO nanotubes and monolayers with 5-aminolevulinic acid drugs as possible nanocarriers for drug delivery: a DFT based molecular dynamic simulation, *Phys. Chem. Chem. Phys.*, 2023, **25**, 21492–21508.
49 N. Sultana, A. Degg, S. Upadhyaya, T. Nilges and N. Sen Sarma, Synthesis, modification, and application of black phosphorus, few-layer black phosphorus (FLBP), and phosphorene: a detailed review, *Mater. Adv.*, 2022, **3**, 5557–5574.
50 Aaryashree, P. V. Shinde, A. Kumar, D. J. Late and C. S. Rout, Recent advances in 2D black phosphorus based materials for gas sensing applications, *J. Mater. Chem. C*, 2021, **9**, 3773–3794.
51 H. H. Liu, Z. M. Su and H. L. Xu, One electron into the multilayer cyclic hexamer of hydrogen fluoride, *J. Fluorine Chem.*, 2025, **283–284**, 110429.
52 K. Hossain, M. T. Ahmed, R. A. Rabu and F. Ahmed, First-principles investigations of As-doped tetragonal boron nitride nanosheets for toxic gas sensing applications, *Nanoscale Adv.*, 2024, 354–369.
53 M. Izadkhah, H. Erfan-niya and S. Z. Heris, Influence of graphene oxide nanosheets on the stability and thermal conductivity of nanofluids Insights from molecular dynamics simulations, *J. Therm. Anal. Calorim.*, 2018, **7**, 581–595.
54 H. He, L. Li, R. Ya, H. Liu, B. Luo, Z. Li and W. Tian, Molecular dynamics simulation and experimental verification of the effects of vinyl silicone oil viscosity on the mechanical properties of silicone rubber foam, *RSC Adv.*, 2024, **14**, 23840–23852.
55 J. Fu, B. Wang, Y. Chen, Y. Li, X. Tan, B. Wang and B. Ye, Computational analysis the relationships of energy and mechanical properties with sensitivity for FOX-7 based PBXs via MD simulation, *R. Soc. Open Sci.*, 2021, **8**, 200345.

56 S. U. D. Shamim, T. Hussain, M. R. Hossian, M. K. Hossain, F. Ahmed, T. Ferdous and M. A. Hossain, A DFT study on the geometrical structures, electronic, and spectroscopic properties of inverse sandwich monocyclic boron nanoclusters Co_nB_m (n = 1.2; m = 6–8), *J. Mol. Model.*, 2020, **26**, 1–17.

57 J. Mawwa, S. U. D. Shamim, S. Khanom, M. K. Hossain and F. Ahmed, In-plane graphene/boron nitride heterostructures and their potential application as toxic gas sensors, *RSC Adv.*, 2021, **11**, 32810–32823.

58 M. T. Ahmed, A. Al Roman, D. Roy, S. Islam and F. Ahmed, Phosphorus-doped T-graphene nanocapsule toward O_3 and SO_2 gas sensing: a DFT and QTAIM analysis, *Sci. Rep.*, 2024, **14**, 1–18.

59 S. Lata, P. K. Singh and S. R. Samadder, Regeneration of adsorbents and recovery of heavy metals: a review, *Int. J. Environ. Sci. Technol.*, 2015, **12**, 1461–1478.

60 S. Hasan, M. T. Ahmed, A. Al Roman, S. Islam and F. Ahmed, Investigation of Structural, Electronic, and Optical Properties of Chalcogen-Doped ZrS_2: A DFT Analysis, *Adv. Mater. Sci. Eng.*, 2023, **2023**, 6525507.

61 J. Mawwa, S. U. D. Shamim, S. Khanom, M. K. Hossain and F. Ahmed, In-plane graphene/boron nitride heterostructures and their potential application as toxic gas sensors, *RSC Adv.*, 2021, **11**, 32810–32823.

62 F. Nazneen, N. Z. Tanwee, N. A. Shahed, S. Khanom, K. Hossain, J. I. Khandaker, F. Ahmed and M. A. Hossain, Ab initio study of P-doped borocarbonitride nanosheet as anode material for Li-ion and Na-ion batteries, *Mater. Today Commun.*, 2020, **25**, 101409.

63 W. Kream Alaarage, A. H. Abo Nasria and A. H. Omran Alkhayatt, A DFT investigation of an InP bilayer: A potential gas sensor with promising adsorption and optical response, *Comput. Theor. Chem.*, 2023, **1227**, 114223.

64 A. Talha, F. H. Shihab, M. T. Ahmed, A. Al Roman, Z. Kowser and D. Roy, Density functional theory study of the adsorption and dissociation of OF_2 and O_3 gases on the surface of pristine and Al, Ti and Cr doped graphene, *AIP Adv.*, 2024, **14**, 75008.

65 R. Vargas-Bernal, Electrical Properties of Two-Dimensional Materials Used in Gas Sensors, *Sensors*, 2019, **19**, 1295.

66 P. Ou, P. Song, X. Liu and J. Song, Superior Sensing Properties of Black Phosphorus as Gas Sensors: A Case Study on the Volatile Organic Compounds, *Adv. Theory Simul.*, 2019, **2**, 1800103.

67 V. V. Kulish, O. I. Malyi, C. Persson and P. Wu, Adsorption of metal adatoms on single-layer phosphorene, *Phys. Chem. Chem. Phys.*, 2015, **17**, 992–1000.

68 C. Wang, Q. Xia, Y. Nie and G. Guo, Strain-induced gap transition and anisotropic Dirac-like cones in monolayer and bilayer phosphorene, *J. Appl. Phys.*, 2015, **117**, 124302.

69 H. Liu, A. T. Neal, Z. Zhu, Z. Luo, X. Xu, D. Tománek and P. D. Ye, Phosphorene: An unexplored 2D semiconductor with a high hole mobility, *ACS Nano*, 2014, **8**, 4033–4041.

70 R. Khatun, M. T. Ahmed, S. Islam, M. K. Hossain, M. A. Hossain and F. Ahmed, First-principles investigation of hexagonal boron-carbon-nitride (h-BCN) nanosheet (2D) as gas sensor towards toxic gases (CO, H_2S, PH_3, SO_2, and HCN), *Int. J. Comput. Mater. Sci. Surf. Eng.*, 2021, **10**, 184.

71 A. S. Rad, N. Nasimi, M. Jafari, D. S. Shabestari and E. Gerami, Ab-initio study of interaction of some atmospheric gases (SO_2, NH_3, H_2O, CO, CH_4 and CO_2) with polypyrrole (3PPy) gas sensor: DFT calculations, *Sens. Actuators, B*, 2015, **220**, 641–651.

72 D. Guedes-Sobrinho, C. R. Caldeira Rêgo, G. R. Da Silva, H. R. Da Silva, W. Wenzel, M. J. Piotrowski and A. Cavalheiro Dias, Theoretical Exploration of Structural and Excitonic Properties in Black Phosphorus: From First-Principles to a Semi-Empirical Approach, *J. Phys. Chem. C*, 2024, **128**, 7242–7251.

73 Y. Oh, S. Song and J. Bae, A Review of Bandgap Engineering and Prediction in 2D Material Heterostructures: A DFT Perspective, *Int. J. Mol. Sci.*, 2024, **25**, 13104.

74 K. Hossain, M. T. Ahmed, R. A. Rabu and F. Ahmed, First-principles investigations of As-doped tetragonal boron nitride nanosheets for toxic gas sensing applications, *Nanoscale Adv.*, 2024, **7**, 354–369.

75 A. Kobayashi, S. Katayama and Y. Suzumura, Theoretical study of the zero-gap organic conductor α-$(BEDT\text{-}TTF)_2I_3$, *Sci. Technol. Adv. Mater.*, 2009, **10**, 024309.

76 J. Li, H. Zhao, Y. Wang and Y. Zhou, Approaches for selectivity improvement of conductometric gas sensors: an overview, *Sens. Diagn.*, 2024, **3**, 336–353.

77 J. H. Li, J. Wu and Y. X. Yu, DFT exploration of sensor performances of two-dimensional WO_3 to ten small gases in terms of work function and band gap changes and I-V responses, *Appl. Surf. Sci.*, 2021, **546**, 149104.

78 M. G. Muktadir, A. Alam, A. A. Piya and S. U. D. Shamim, Exploring the adsorption ability with sensitivity and reactivity of C_{12}–B_6N_6, C_{12}–Al_6N_6, and B_6N_6–Al_6N_6 heteronanocages towards the cisplatin drug: a DFT, AIM, and COSMO analysis, *RSC Adv.*, 2022, **12**, 29569–29584.

79 X. Peng, D. Liu, F. Zhao and C. Tang, Gas sensing properties of Mg-doped graphene for H_2S, SO_2, SOF_2, and SO_2F_2 based on DFT, *Int. J. Quantum Chem.*, 2022, **122**, e26989.

80 M. Rezvani, M. Astaraki, A. Rahmanzadeh and M. Darvish Ganji, Theoretical assessments on the interaction between amino acids and the g-Mg_3N_2 monolayer: dispersion corrected DFT and DFT-MD simulations, *Phys. Chem. Chem. Phys.*, 2021, **23**, 17440–17452.

81 H. M. Ng, T. D. Moustakas and S. N. G. Chu, High reflectivity and broad bandwidth AlN/GaN distributed Bragg reflectors grown by molecular-beam epitaxy, *Appl. Phys. Lett.*, 2000, **76**, 2818–2820.

82 Y. x. Li, S. s. Chen and F. d. Ren, Theoretical insights into the structures and mechanical properties of HMX/NQ cocrystal explosives and their complexes, and the influence of molecular ratios on their bonding energies, *J. Mol. Model.*, 2015, **21**, 1–12.

83 H. F. Gao, S. H. Zhang, F. De Ren, F. Liu, R. J. Gou and X. Ding, Theoretical insight into the co-crystal explosive of 2,4,6,8,10,12-hexanitrohexaazaisowurtzitane (CL-20)/1,1-diamino-2,2-dinitroethylene (FOX-7), *Comput. Mater. Sci.*, 2015, **107**, 33–41.

84 X. D. D. Dexlin, J. D. D. Tarika, S. M. Kumar, A. Mariappan and T. J. Beaula, Synthesis and DFT computations on structural, electronic and vibrational spectra, RDG analysis and molecular docking of novel Anti COVID-19 molecule 3,5-Dimethyl Pyrazolium 3,5-Dichloro Salicylate, *J. Mol. Struct.*, 2021, **1246**, 131165.

85 D. Raval, S. K. Gupta and P. N. Gajjar, Detection of H_2S, HF and pollutant gases on the surface of penta-$PdAs_2$ monolayer using DFT approach, *Sci. Rep.*, 2023, 1–10.

86 L. Chhana, B. Lalroliana, R. C. Tiwari, B. Chettri, L. Pachuau, S. Gurung, L. Vanchhawng, D. P. Rai and L. Zuala, Theoretical Study of ZnS Monolayer Adsorption Behavior for CO and HF Gas, *Molecules*, 2022, **7**, 40176–40183.

87 Y. Wang, S. Guo, X. Xu, J. Pan, J. Hu and S. Zhang, Adsorption and sensing performance of air pollutants on a β-TeO_2 monolayer: a first-principles study, *Phys. Chem. Chem. Phys.*, 2023, **26**, 612–620.

88 R. Gao, Y. Yong, X. Yuan, S. Hu, Q. Hou and Y. Kuang, First-Principles Investigation of Adsorption Behaviors and Electronic, Optical, and Gas-Sensing Properties of Pure and Pd-Decorated GeS_2 Monolayers, *ACS Omega*, 2022, **7**, 46440–46451.

89 S. Pervaiz, M. U. Saeed, H. Ali, Y. Saeed, A. Khan and Y. M. Alanazi, Monolayer CuBr-based gas sensor to detect habitat and industry-relevant molecules with high sensitivity and selectivity: a first-principles study, *RSC Adv.*, 2025, **15**, 16076–16087.

90 K. Hossain, M. T. Ahmed, R. A. Rabu and F. Ahmed, First-principles investigations of As-doped tetragonal boron nitride nanosheets for toxic gas sensing applications, *Nanoscale Adv.*, 2024, **7**, 354–369.

91 R. Majidi and A. Ramazani, Detection of HF and H_2S with pristine and Ti-embedded twin graphene: A density functional theory study, *J. Phys. Chem. Solids*, 2019, **132**, 31–37.